Berg Huettenmaenn Monatsh (2019) Vol. 164 (3): 101–107
https://doi.org/10.1007/s00501-019-0828-y

BHM Berg- und Hüttenmännische Monatshefte

Feasability Investigation for Laser Powder Bed Fusion of High-Speed Steel AISI M50 with Base Preheating System

Jasmin Saewe[1], Christoph Gayer[1], Andreas Vogelpoth[1], and Johannes Henrich Schleifenbaum[1,2]

[1]Fraunhofer Institute for Laser Technology (ILT), Aachen, Germany
[2]Digital Additive Production, RWTH Aachen University (DAP), Aachen, Germany

Received January 14, 2019; accepted January 24, 2019; published online February 14, 2019

Abstract: Laser Powder Bed Fusion (LPBF) is an additive manufacturing process employed in the aerospace, automotive, and medical industries. In these sectors, nickel-, aluminium-, and titanium-based alloys are mainly used for various applications. Yet, only few of the commonly used steels have been qualified for the LPBF process in the mechanical engineering industry, which normally uses hot work tool steels with less than 0.5 wt.-% carbon content. However, many applications need high wear-resistant steel alloys with high hardness, both of which can be achieved with a higher carbon content, like in high-speed steels. But when processed with LPBF, these steels often form cracks, making the process very challenging.

In this feasibility investigation, we demonstrate that LPBF can be used to manufacture dense and crack-free specimens with a hardness of over 62 HRC (as built) from high-speed steel AISI M50 (carbon content of 0.8 wt.-%). Furthermore, we evaluate the influence of typical LPBF process parameters, especially of preheating temperatures up to 500 °C, on the microstructure of the specimens.

Keywords: LPBF, Laser Powder Bed Fusion, SLM, Selective Laser Melting, High-speed steel, High carbon content, Preheating, M50, Bearing steel, Tool steel

Machbarkeitsstudie für das Laser Powder Bed Fusion von Schnellarbeitsstahl AISI M50 mit einem Substratplattenvorheizsystem

Zusammenfassung: Laser Powder Bed Fusion (LPBF) ist ein additives Fertigungsverfahren, welches in der Luft- und Raumfahrt, der Automobilindustrie und der Medizintechnik eingesetzt wird. In diesen Bereichen werden hauptsächlich Nickel-, Aluminium- und Titanbasislegierungen für verschiedene Anwendungen eingesetzt. Doch nur wenige der gängigen Stähle aus der Maschinenbauindustrie sind für den LPBF-Prozess qualifiziert. Bisher werden Warmarbeitsstähle mit weniger als 0,5 gew.-% Kohlenstoffgehalt mittels LPBF verwendet. Viele Anwendungen erfordern jedoch verschleißfestere Stahllegierungen mit hoher Härte, die nur mit einem höheren Kohlenstoffgehalt erreicht werden können, beispielsweise bei Schnellarbeitsstählen. Bei der Verarbeitung mittels LPBF bilden diese Stähle jedoch oft Risse.

In dieser Machbarkeitsstudie wird gezeigt, dass LPBF zur Herstellung von dichten und rissfreien Proben mit einer Härte von über 62 HRC (as built) aus Schnellarbeitsstahl AISI M50 (Kohlenstoffgehalt von 0,8 gew.-%) verwendet werden kann. Darüber hinaus wird der Einfluss typischer LPBF-Prozessparameter, insbesondere von Vorwärmtemperaturen bis 500 °C, auf die Mikrostruktur der Proben untersucht.

Schlüsselwörter: LPBF, Laser Powder Bed Fusion, SLM, Selective Laser Melting, Schnellarbeitsstahl, Werkzeugstahl, Kohlenstoffgehalt, Vorheizung, M50, Wälzlagerstahl

1. Introduction

Laser Powder Bed Fusion (LPBF), also known as Selective Laser Melting (SLM), is an Additive Manufacturing (AM) process used in multiple industries, such as aerospace, automotive, and medical engineering [1–3]. In this process, metal powder is melted layer by layer with a focused laser beam that melts selected areas to fuse the material into a 3D part [4]. The multiple advantages of this process are also interesting for rolling bearings where for example a flexible design of the outer geometries can be achieved with LPBF. When used to produce bearings, LPBF makes it possible to easily adapt to surrounding parts and to increase the degree of integration, both of which lead to new lightweight designs. Moreover, there is a great demand for economical and near-net-shape production to facilitate the next step in the machining process.

J. Saewe, M.Sc. (✉)
Fraunhofer Institute for Laser Technology (ILT),
Steinbachstr. 15,
52074 Aachen, Germany
jasmin.saewe@ilt.fraunhofer.de

Most steels commonly used with LPBF are austenitic stainless steels AISI 316L (EN 1.4404) and AISI 304L (EN 1.4306), maraging steel 1.2709 or hardenable stainless steels 17-4 PH (EN 1.4545) and 15-5 PH (EN 1.4548) [2, 5, 6]. But these alloys have insufficient wear resistance and, therefore, cannot be used in the production of rolling bearings as they would not withstand the loads. Bearing steels are special tool steels and are commonly used for this application. These steels have similar properties as high-speed steels and are suitable for the operating conditions to which a rolling bearing is subjected. But these steels often have a high carbon content (>0.4 wt.-%) and are considered as unweldable.

Up to now there have been few publications about LPBF of high-speed steel or high carbon steels [7–10]. Kempen, et al. [7] investigate how the preheating temperature influences the part density and the tendency of tool steel M2 (1.3343) with a carbon content of 0.9% to crack. With a preheating temperature of 200 °C, they are able to build dense components (99.8%) crack-free using LPBF. Liu, et al. [8] process M2 at room temperature and a preheating temperature of 180 °C. With preheating, M2 can be manufactured without cracks and with a part density greater than 99.7%. Furthermore, the authors demonstrate different microstructures with varying hardness within a melt lens and reach a hardness of over 800 HV. In [9] , Zumofen, et al. investigate the influence of the preheating temperature on component distortion due to residual stresses by manufacturing cantilevers from M2. The manufacture of the cantilevers at a preheating temperature of 400 °C reduces component distortion.

Since LPBF has such high cooling rates (up to 10^6 K/s [11]), the material solidifies rapidly, which results in fine microstructures and higher strength [12]. The temperature gradients in the process create grain growth in the build direction, which can cause brittleness and encourages crack formation [13]. The use of a preheating system for the base plate is a promising approach for reducing the temperature gradient and internal stresses of parts.

This paper focuses on the high-speed steel (bearing steel) AISI M50, also known as 1.3551 or 80MoCrV42-16, with 0.8 wt.-% carbon content. M50 is used in the rolling bearing industry in conventional production as a standard material [14]. It is a suitable alloy for rolling bearings due to the high initial hardness after martensitic hardening and high-temperature strength. This paper presents research on how the LPBF process parameters, in particular the laser power, influence hardness. In addition, it evaluates the influence of the base plate preheating temperature of 200 °C and 500 °C on the microstructure of the specimens.

2. Material and Methods

For this study the high-speed steel AISI M50 (80MoCrV42-16) was used. The chemical composition of the powder is shown in Table 1.

The particle size distribution (PSD) of AISI M50 powder in Fig. 1a is evaluated by optical analysis of Malvern Morphologi G3 to d_{10} = 21.7 µm, d_{50} = 32.3 µm and d_{90} = 47.5 µm. The particles are mainly spherical (Fig. 1b), but some pores were detected within the powder cross-section (Fig. 1c).

To build the test specimens, a modified laboratory LPBF machine from Aconity3D was used, equipped with a fiber laser with a wavelength of 1064 nm, a maximum output power of 400 W, and a 3D scan system from Scanlab (varioSCAN40 and intelliSCAN20). The laser spot has a Gaussian shape with 80 µm diameter ($1/e^2$) in the focal plane. The resistance preheating system can heat the base plate up to 800 °C.

The volume energy density E_V (Eq. 1) can be used to compare the theoretical energy input of the laser beam into the material for different process parameters. The process parameters laser power P_L, scan velocity v_s, hatch distance Δy_s as well as layer thickness D_s influence the energy input [4].

$$E_V = \frac{P_L}{v_s \cdot \Delta y_s \cdot D_s} \tag{1}$$

Table 1
Chemical Composition of M50 (as in datasheet [15])

Chemical Elements [wt.-%]	C	Si	Mn	Cr	Mo	V	Fe
M50 (1.3551, 80MoCrV42-16)	0.83	0.2	0.25	4.0	4.3	1.05	Balanced

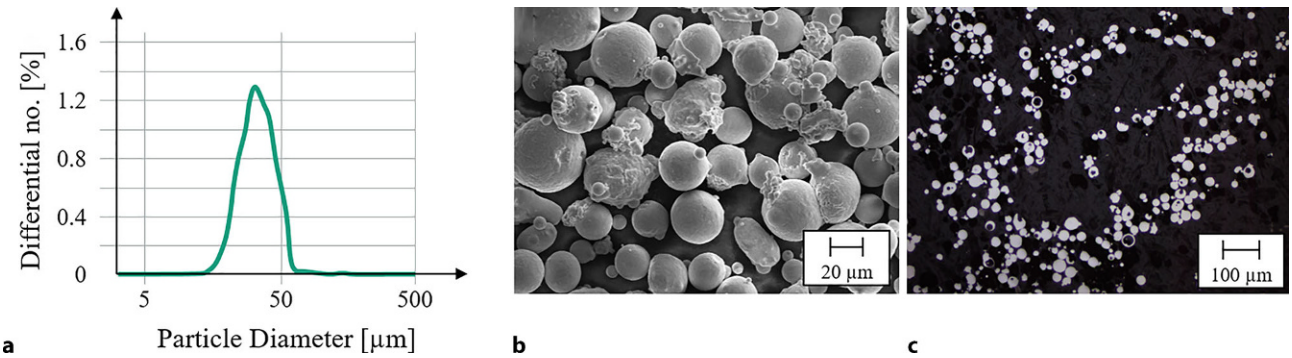

Fig. 1: Particle size distribution (**a**), SEM image (**b**), and light optical micrograph (LOM) of cross-section (**c**) of powder AISI M50

$P_{L,1}$ = 130 W			
$T_{H,1}$ = RT, $T_{H,2}$ = 200 °C, $T_{H,3}$ = 500 °C			
Part No.	Δy_s [µm]	v_s [mm/s]	E_V [J/mm³] (rounded)
1A	60	800	90
2A		900	80
3A		1035	70
4A	80	600	90
5A		675	80
6A		775	70
7A		900	60
8A	100	480	90
9A		540	80
10A		620	70
11A		720	60
12A	120	400	90
13A		450	80
14A		520	70

a

$P_{L,2}$ = 260 W			
$T_{H,1}$ = RT			
Part No.	Δy_s [µm]	v_s [mm/s]	E_V [J/mm³] (rounded)
1B	60	1450	100
2B		1600	90
3B		1800	80
4B	80	1080	100
5B		1200	90
6B		1350	80
7B		1550	70
8B	100	860	100
9B		960	90
10B		1080	80
11B		1250	70
12B	120	720	100
13B		800	90
14B		900	80

b

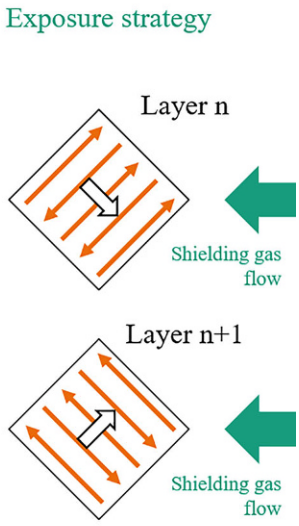

c

Fig. 2: Table of process parameter variation for $P_{L,1}$ = 130 W (**a**) $P_{L,2}$ = 260 W (**b**), and schematic exposure strategy (**c**)

The experiments were carried out under an argon inert-gas atmosphere with an oxygen content below 100 ppm at approx. 50 mbar overpressure compared to the ambient atmosphere. As process parameters, a layer thickness of 30 µm and a laser power of $P_{L,1}$ = 130 W or $P_{L,2}$ = 260 W were kept constant throughout the experiments. The other process parameters were varied as can be seen in Fig. 2a and 2b. First, the experiments were carried out without preheating ($T_{H,1}$ = RT (room temperature)). For $P_{L,1}$ and $P_{L,2}$, the experiment compared how process parameters influenced the processability, hardness, and microstructure. Subsequently, the base plate was heated up to $T_{H,2}$ = 200 °C and $T_{H,3}$ = 500 °C for $P_{L,1}$.

A zig-zag pattern (also called meandering) with an alternating hatch rotation of 90 degrees per layer was used as exposure strategy (Fig. 2c). Test specimens with a dimension of 10 × 10 × 10 mm³ were manufactured for part density and microstructure evaluation.

The specimens were cut from the build plate by electrical discharge machining (EDM) wire cutting. To determine the part density, the polished cross-section was analysed using light optical microscopy (LOM). The polished specimens were etched with nitric acid (10% HNO_3) to visualize the microstructure of the test specimens. The hardness was measured with HV0.3 according to DIN EN ISO 6507 with a minimum of 25 points. The scanning electron microscope (SEM) images were captured using a LEO 1455 EP (Zeiss).

3. Results and Discussion

Fig. 3 shows the cross-sections of specimens built with laser power $P_{L,1}$ = 130 W and $P_{L,2}$ = 260 W. The specimens in Fig. 3 were built with a volume energy density of E_V = 70 J/mm³ and without using a preheating system ($T_{H,1}$ = RT). The test specimens built with $P_{L,1}$ (Fig. 3a) have a part density above 99.9% and show a mostly homogeneous distribution of very few spherical pores. There are cracks visible in the cross-sections, which start either at the bottom or at the top of the specimen. In Fig. 3b the cross-sections built with $P_{L,2}$ and the separation into two zones are shown. Zone 1 shows high porosity, which can be identified mostly as lack of fusion. In Zone 2 the part density is above 99.9% and very few pores can be detected, which are homogeneously distributed and spherical. In both zones no cracks were observed.

The cracks in specimen 6A (Fig. 3a) from the bottom are mostly caused by the support structure to the base plate, which can trigger cracks because of a notch effect. The cracks in specimen 10A were caused by cutting the part for the cross-section analysis. The force of the cutting tool can cause the inner tensions of the material to initiate cracks.

Fig. 3b shows cross-sections of specimens manufactured with two different settings of shielding gas flow. The flow velocity was adjusted by the pump circulation power from 50% in Zone 1 to 70% in Zone 2. The process parameters were kept constant for each specimen (7B and 11B). In Zone 1 the lower pump power caused a low shielding gas flow, and the spatters and plume of the process were not carried away by the flow. This caused low part density. Only by adjusting the pump power in Zone 2 could a high part density be achieved. This shows the high influence of shielding gas flow on part quality as shown in many publications [13, 16, 17].

The hardness measured for all specimens with $P_{L,1}$ = 130 W and $P_{L,2}$ = 260 W is shown in Fig. 4. With constant laser power, the different hatch distances of 60 to 120 µm as well as the volume energy density of 60 to 100 J/mm³ have no significant influence on the hardness. The mean hardness of specimens built with $P_{L,1}$ is approx. 728 ± 46 HV

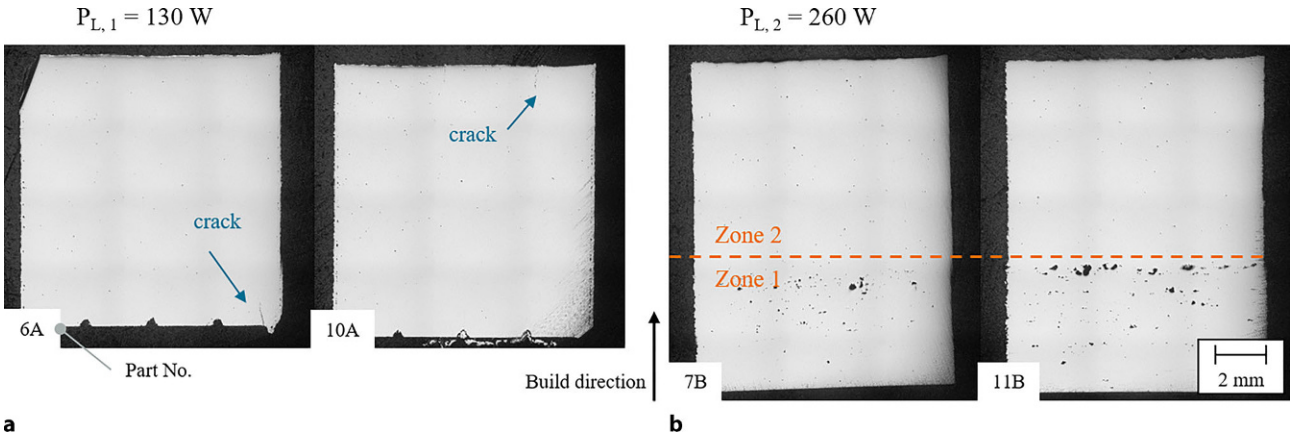

Fig. 3: Cross-section of specimens built with $P_{L,1}$ (**a**) and $P_{L,2}$ (**b**) with volume energy density of 70 J/mm^3 and hatch distance of 80 µm (6A, 7B) and 100 µm (10A, 11B) at $T_{H,1}$ = RT

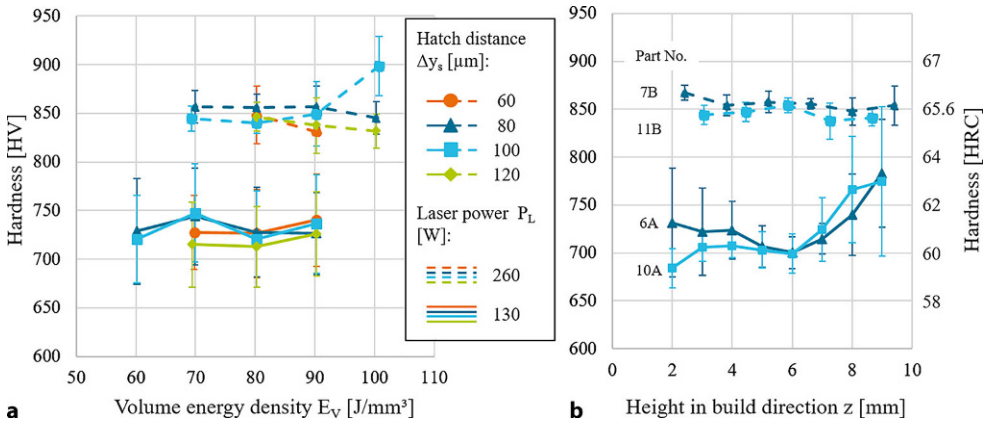

Fig. 4: Comparison of hardness of specimens built with $P_{L,1}$ and $P_{L,2}$ (**a**) and hardness over part height z (**b**) for specimens built with volume energy density of 70 J/mm^3 and hatch distance of 80 µm (6A, 7B) and 100 µm (10A, 11B) at $T_{H,1}$ = RT

(61.2 HRC). The specimens built with $P_{L,2}$ reach a mean value of 849 ± 21 HV (65.6 HRC).

In Fig. 4b the hardness of specimens built with $P_{L,1}$ and $P_{L,2}$ is shown over part height z. The hardness of the specimens built with $P_{L,1}$ (6A and 10A) is constant below 750 HV for $z \leq 7$ mm. For $z > 7$ mm the hardness increases up to 783 ± 56 HV for specimen 6A and 774 ± 78 HV for 10A. The hardness for specimens 7B and 11B built with $P_{L,2}$ is independent of part height z. The mean hardness for specimen 7B is 854 ± 13 HV and 845 ± 11 HV for 11B.

Even with the same volume energy input, the specimens show a significantly different hardness when built with $P_{L,1}$ or $P_{L,2}$. Due to this result, it can be assumed that different heat treatment effects apply over part height during the process depending on the process parameters. The specimens built with $P_{L,1}$ and $P_{L,2}$ were built separately in two build jobs. To have the same energy input in form of theoretical volume energy density, the specimens with $P_{L,2} = 2 * P_{L,1}$ and hatch distance $\Delta y_{s,2} = \Delta y_{s,1}$ need to be exposed with doubled scan speed $v_{s,2} = 2 * v_{s,1}$. This leads to a higher theoretical build-up rate, which in turn leads to a faster build-up for the build job with $P_{L,2}$. The build job with $P_{L,1}$ took approx. 4 h process time, while the job with $P_{L,2}$ only took approx. 2.5 h. Even with no preheating, the jobs were built on the preheating module (switched off), which has a poor heat transfer downwards due to the ceramic seals. This can lead to higher heat accumulations during the process compared to build jobs on machines with a normal base plate without seals.

During the build job with $P_{L,1}$, the specimens were exposed to the heat of the process for a longer period of time. Since the layers at lower part height are exposed to the heat input of the layers above, the hardness is different to the layers at higher z, where fewer layers are on top and, therefore, less heat can be effective for less time. The heat accumulation in the specimen for $z \leq 7$ mm during the build job can be assumed to be above the martensite starting temperature of approx. 200 °C [18].

The specimens built with $P_{L,2}$ were exposed faster and had less time to cool down in each layer. Because of the faster build job, the duration of heat accumulation at the lower area is shorter. Since the hardness is constant and the structure through the specimen is homogeneous, it can be assumed that the heat input due to the laser and the heat accumulation result in balanced heat of the entire specimen. Also, lower temperatures in the parts with $P_{L,2}$ compared to $P_{L,1}$ are assumed because of the higher constant hardness.

Fig. 5 shows the etched cross sections of the specimens built with $P_{L,1}$ (10A) and $P_{L,2}$ (11B) at two different part heights (upper area: $z \approx 9$ mm and lower area: $z \approx 2$ mm). By etching the cross sections, the microstructure and melt track boundaries are revealed and exemplary marked.

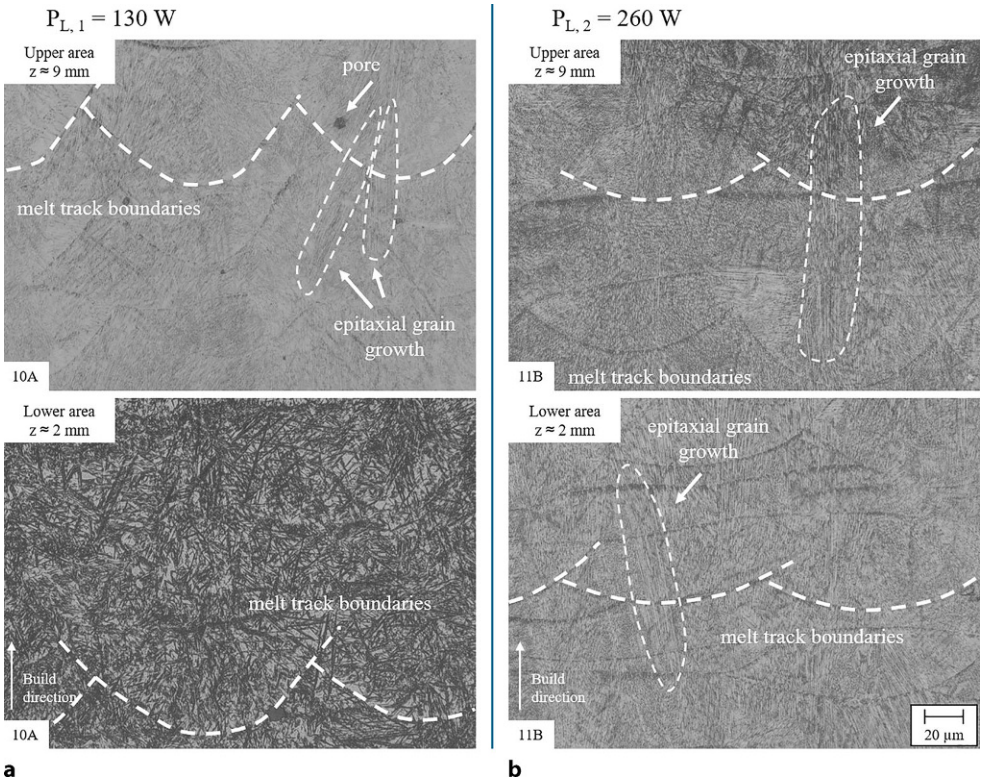

Fig. 5: LOM of etched cross-sections at different part height z of two specimens (10A, 11B) built with $P_{L,1}$ (**a**) and $P_{L,2}$ (**b**) with volume energy density of 70 J/mm^3 and hatch distance of 100 µm

In the upper area of 10A in Fig. 5a, columnar dendritic structures are visible that grow over several layers. This is an indication of epitaxial grain growth during the process, where grains growing in the direction of the thermal gradient through the melt track boundaries. The lower area of the same specimen shows clear martensite-dominated structure. Between the martensite needles, small fractions of retained austenite are visible.

In Fig. 5b specimen 11B has similar structures in the upper and lower areas. The regularly allocated dendrite structure and again columnar dendrites grown above melt track boundaries can be observed in both part heights and are more distinct compared those seen in Fig. 5a.

The course of hardness over part height in Fig. 4b can be compared to the microstructure of the etched cross-sections in Fig. 5. Specimens built with $P_{L,1}$ seem to be exposed to an inhomogeneous heat, which leads to different structures and increasing hardness over part height. For specimens built with $P_{L,2}$, the heat during the process is assumed to be more homogeneously distributed, meaning the microstructure is similar and hardness is constant over part height.

For the next two experiments, the laser power of $P_{L,1}$ = 130 W was kept constant while the preheating temperature was varied to $T_{H,2}$ = 200 °C and $T_{H,3}$ = 500 °C. The part density of the specimens is above 99.5%. The mean hardness of all specimens built at $T_{H,2}$ is 722 ± 42 HV (61 HRC). For specimens built at $T_{H,3}$, the mean value is 792 ± 50 HV (63.7 HRC). No significant influence of volume energy density or hatch distance was observed.

Fig. 6 shows the hardness over part height for four specimens with two process parameters (6A, 10A). The hardness over part height for specimens built at 200 °C in Fig. 6a is similar to the hardness of specimens built at RT. The hardness is around 700 HV for z < 4 mm, and the standard deviation for z < 6 mm is smaller compared to $T_{H,1}$. The hardness increases at z > 8 mm to over 750 HV for specimen 10A and over 800 HV for specimen 6A at $T_{H,2}$. Fig. 6b shows the hardness over part height of specimens 6A and 10A built at $T_{H,3}$. The hardness increases linearly from approx. 750 HV at z < 2 mm to 850 HV at z > 8 mm.

The last layers are exposed to lower preheating temperatures because of heat transfer losses, which lead to a thermal gradient where the temperature decreases with increasing part height. This is caused by the preheating system, which is located in the base plate and transmits only limited heat into upper areas of the specimen. The energy input of the laser in each layer is too low to maintain the temperature in the specimen over part height. Therefore, there are no constant temperatures assumed over part height which lead to varying hardness in the specimens.

Again, the hardness indicates heat accumulations and heat transfer within the specimen during the process. The hardness of $T_{H,1}$ (Fig. 4b) and $T_{H,2}$ (Fig. 6a) is similar in lower areas. By preheating the base plate to 200 °C and heat input from layers above, the temperature in the lower area is assumed to be ≥200 °C for $T_{H,2}$. The preheating causes stable temperature conditions, which can be indicated by lower standard deviations of hardness shown in Fig. 6. Since at $T_{H,1}$ no preheating temperatures are applied, the heat accumulation slowly builds up with the energy input from the above layers. Therefore, the temperature conditions are unstable at the lower area. But since the hardness of $T_{H,1}$ and $T_{H,2}$ is similar, this also indicates that the tem-

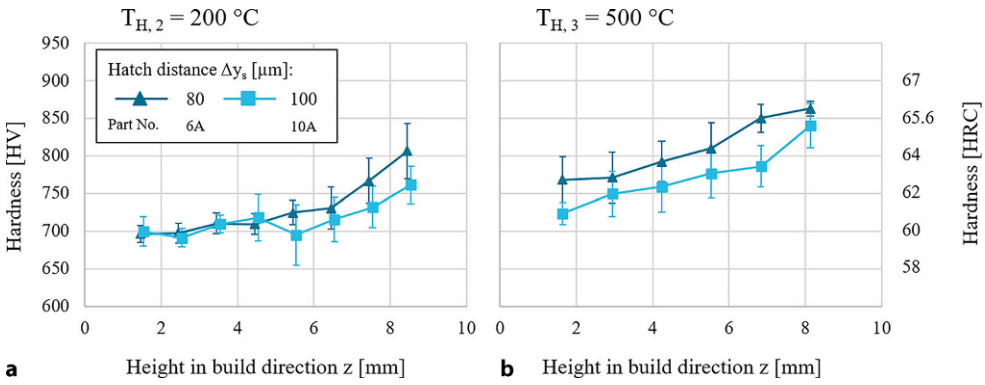

Fig. 6: Measured hardness over part height z for specimens built with $P_{L,1}$ = 130 W at preheating temperature $T_{H,2}$ = 200 °C (**a**) and $T_{H,3}$ = 500 °C (**b**) with volume energy density of 70 J/mm^3 and hatch distance of 80 µm (6A) and 100 µm (10A)

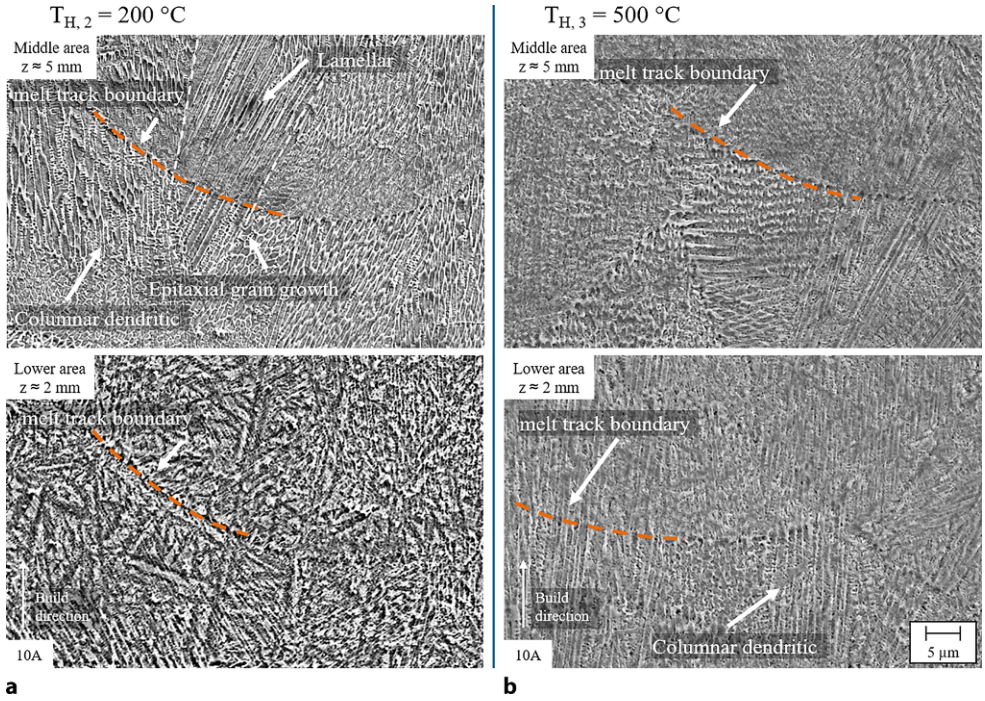

Fig. 7: SEM images of etched cross-sections of specimens built with $P_{L,1}$ at preheating temperature $T_{H,2}$ = 200 °C (**a**) and $T_{H,3}$ = 500 °C (**b**) with volume energy density of 70 J/mm^3 and hatch distance of 100 µm (10A)

perature in the lower area of specimens built at $T_{H,1}$ is approx. 200 °C.

The hardness for $T_{H,3}$ = 500 °C has a different behaviour. The constant high temperature during the build job of 4 h can lead to bainitic microstructures regarding the time-temperature-transformation (TTT) diagram in [18]. This can cause the linear course to higher hardness over part height. The temperature range also favours the formation of secondary carbides.

Fig. 7 shows the SEM images of etched cross-sections of specimen 10A for two different part heights at preheating temperatures $T_{H,2}$ = 200 °C and $T_{H,3}$ = 500 °C.

For $T_{H,2}$ the SEM image in Fig. 7a illustrates the differences in microstructure over part height. The middle area shows a dendritic structure. For the lower area, a needle-like structure together with a dendritic structure can be observed. The grain structure is very homogeneously distributed. Compared to the middle area, the lower area has a coarser structure, which can be triggered by diffusion processes.

In Fig. 7b the SEM images of specimen 10A built at $T_{H,3}$ is shown. In the lower area, columnar dendritic structures that grow over several layers can be observed. In the middle area of the specimen, the columnar dendritic structure is more distinct than in the lower area.

The microstructure seen in Fig. 7a is significantly heat treated in the lower area with a more homogeneous microstructure. The microstructure is clearly different for both heights in the SEM images, when compared to the hardness in Fig. 6a, in which the hardness is comparable at part height z = 2 mm and z = 5 mm. The microstructure in Fig. 7b is difficult to compare with the hardness in Fig. 6b. Due to the preheating temperature, the microstructure differs strongly between lower and upper area, as expected. Due to the high temperatures over the long process time, a bainitic microstructure can be assumed.

4. Conclusion

In this study, the material M50 was processed without preheating at two different laser powers ($P_{L,1}$ = 130 W and $P_{L,2}$ = 260 W) and with preheating temperatures up to 500 °C ($T_{H,1}$ = RT, $T_{H,2}$ = 200 °C, $T_{H,3}$ = 500 °C). In all build jobs, the specimens have a part density over 99.5% and only few defects as cracks were observed at $T_{H,1}$, which are caused by the support structures (notch effects) or the cutting strategy for the material analysis. No cracks were observed at $T_{H,2}$ and $T_{H,3}$.

The influence of the process parameters besides preheating temperatures is visible in the hardness and microstructure of the specimens. Even with a similar volume energy density, the hardness is significantly higher at $P_{L,2}$ (849 HV, 65.6 HRC) compared to $P_{L,1}$ (728 HV, 61.2 HRC). For $P_{L,1}$ the part height influences the hardness, so with increasing part height, the hardness increases as well. This behaviour is explained by heat accumulation due to insulation of the base plate and the energy input of the laser as well as by the process duration of 4 hours compared to 2.5 hours with $P_{L,2}$. The heat in specimens built with $P_{L,2}$ is assumed to be very homogeneous because of the constant hardness and the similar microstructure over part height.

At the preheating temperature of $T_{H,2}$ = 200 °C, the specimens built with $P_{L,1}$ have a mean hardness of 722 HV (61 HRC) and show a similar behaviour in hardness over part height as for $T_{H,1}$. Therefore, a temperature of 200 °C in lower areas of the specimens at $T_{H,1}$ can be emphasized. The temperature gradient leads to decreasing temperatures and higher cooling rates as well as increasing hardness in higher part heights. By preheating to $T_{H,3}$ = 500 °C, the mean hardness can be increased to 792 HV (63.7 HRC). The hardness of the specimens linearly increases over part height, and dendrites can be observed in the microstructure of the lower area.

This feasibility study demonstrates that M50 can be processed crack-free at different preheating temperatures and gives insight into how varying process parameters influences material hardness. This is a promising approach for manufacturing roller bearings in the future.

Acknowledgements. This project was carried out with the support of the European Regional Development Fund ERDF under grant number EFRE-800665.

References

1. Schleifenbaum, H.; Diatlov, A.; Hinke, C.; Bültmann, J.; Voswinckel, H.: Direct photonic production: Towards high speed additive manufacturing of individualized goods, Production Engineering, 5 (2011), no 4, pp 359–371
2. Gebhardt, A.: Understanding additive manufacturing: Rapid prototyping, rapid tooling, rapid manufacturing, Munich: Hanser, 2012
3. Frazier, W. E.: Metal Additive Manufacturing: A Review, Journal of Materials Engineering and Performance, 23 (2014), no 6, pp 1917–1928
4. Meiners, W.: Direktes selektives Laser Sintern einkomponentiger metallischer Werkstoffe, Dissertation, Aachen, Techn. Hochsch. 1999
5. Herzog, D; Seyda, V.; Wycisk, E.; Emmelmann, C.: Additive manufacturing of metals, Acta Materialia, 117 (2016), pp 371–392
6. Bourell, D.; Kruth, J.; Leu, M; Levy, G.; Rosen, D.; Beese, A.; Clare, A.: Materials for additive manufacturing, CIRP Annals, 66 (2017), no 2, pp 659–681
7. Kempen, K.; Vrancken, B.; Buls, S.; Thijs, L.; van Humbeeck, J.; Kruth, J.: Selective Laser Melting of Crack-Free High Density M2 High Speed Steel Parts by Baseplate Preheating, Journal of Manufacturing Science and Engineering, 136 (2014), no 6, p 61026
8. Liu, Z. H.; Chua, C. ; Leong, K. ; Kempen, K.; Thijs, L.; Yasa, E.; Van.Humbeeck, J.; Kruth, J.: A preliminary investigation on Selective Laser Melting of M2 high speed steel, in Soares de Lemos, A. C. (ed.): Innovative developments in virtual and physical prototyping: Proceedings of the 5th International Conference on Advanced Research and Rapid Prototyping, Leiria, Portugal, booknumber 257, page 339–346, 2011
9. Zumofen, L.; Beck, C.; Kirchheim, A.; Dennig, H.: Quality Related Effects of the Preheating Temperature on Laser Melted High Carbon Content Steels, in Klahn, Christoph (ed.): Industrializing Additive Manufacturing—Proceedings of Additive Manufacturing in Products and Applications—AMPA2017, Cham: Springer International Publishing, pp 210–219, 2018
10. Taha, M. A.; Yousef, A. ; Gany, K. ; Sabour, H. : On selective laser melting of ultra high carbon steel: Effect of scan speed and post heat treatment, Materialwissenschaft und Werkstofftechnik, 43 (2012), No. 11, pp 913–923
11. Thijs, L.; Montero Sistiaga, M.; Wauthle, R.; Xie, Q.; Kruth, J.; van Humbeeck, J.: Strong morphological and crystallographic texture and resulting yield strength anisotropy in selective laser melted tantalum, Acta Materialia, 61 (2013), no 12, pp 4657–4668
12. Zhao, X.; Chen, J.; Lin, X.; Huang, W.: Study on microstructure and mechanical properties of laser rapid forming Inconel 718, Materials Science and Engineering: A, 478 (2008), no 1-2, pp 119–124
13. Kruth, J. P.; Froyen, L.; van Vaerenbergh, J.; Mercelis, P.; Rombouts, M.; Lauwers, B.: Selective laser melting of iron-based powder, Journal of Materials Processing Technology, 149 (2004), no 1-3, pp 616–622
14. Pritz, L.; Marsoner, S.; Ebner, R.; Fluch, R.; Tatschl, A.; Münzer, R.: Investigation into microstructural changes due to the rolling contact fatigue of the AISI M50 bearing steel, in Brebbia, C. A (ed.): WIT Press Southampton, UK (WIT Transactions on Engineering Sciences), vol 91, pp 35–45, https://doi.org/10.2495/SECM150041, 2015
15. Erasteel GmbH: Schnellarbeitsstahl E M50 http://www.erasteel.com/sites/default/files/media/document/DE_Grade_EM50.pdf (10 July 2018)
16. Ferrar, B.; Mullen, L.; Jones, E.; Stamp, R.; Sutcliffe, C.: Gas flow effects on selective laser melting (SLM) manufacturing performance, Journal of Materials Processing Technology, 212 (2012), no 2, pp 355–364
17. Ladewig, A.; Schlick, G.; Fisser, M.; Schulze, V.; Glatzel, U..: Influence of the shielding gas flow on the removal of process by-products in the selective laser melting process, in Additive Manufacturing, 10 (2016), pp 1–9
18. Kunz, J.; Herzog, S.; Kaletsch, A.; Broeckmann, C.; Saewe, J.; Gayer, C.; Schleifenbaum, J.: Influence of Powder Bed Temperature on Microstructure and Post Heat Treatment of High Speed Steel AISI M50 Processed by Laser Powder Bed Fusion, International Powder Metallurgy Congress and Exhibition, European Powder Metallurgy Association -EPMA-: Euro PM2018 Proceedings : 14 – 18 October 2018, Bilbao, Spain Shrewsbury: EPMA, 2018 ISBN: 978-1-899072-50-7, 6 pp.